

# Robust Control Compensation for Space Descent & Landing\*

Pedro Simplicio<sup>1</sup> and Andrés Marcos<sup>1</sup>  
Eric Joffre<sup>2</sup>, Mattia Zamaro<sup>2</sup> and Nuno Silva<sup>2</sup>

**Abstract**—This paper presents a complete modelling, synthesis and analysis methodology of control compensators for descent and landing on small planetary bodies. These missions are scientifically very rewarding, but also extremely challenging due to the complex and poorly-known environment around those bodies, calling for the ability to manage competing robustness/performance requirements by design. Here, this is achieved using robust control tools and the recently-developed structured  $\mathcal{H}_\infty$  framework. The proposed method is verified for three distinct landing trajectories on the Martian moon Phobos.

## I. INTRODUCTION

A renewed scientific interest has been growing in the exploration of small asteroids in addition to larger planetary bodies such as Mars, since their weaker gravitational field makes them more easily accessible. However, these missions are very challenging from an engineering perspective, particularly if the natural dynamics of the target asteroid is exploited to alleviate descent & landing (D&L) propellant consumption requirements. This is because small bodies are typically characterised by highly irregular and poorly-known shapes, which render their environment extremely uncertain and variable. Moreover, due to the interplanetary distances involved, fully autonomous algorithms are required to cope with communication delays and spacecraft subsystems degradation, as demonstrated by the European Rosetta mission.

As part of the UK Space Agency Technology Programme, the University of Bristol and Airbus Defence and Space were awarded the project "Robust and Nonlinear Guidance and Control for Landing on Small Bodies", with the aim to investigate the application of robust control techniques for the design of D&L guidance and compensation strategies. Although a generic framework was pursued, the project focused on the Martian moon Phobos, which is a strong candidate for an European sample return mission. To reach its goal, a separation between guidance and control compensation schemes (depicted in the block diagram of Fig. 1 and discussed later on) was assumed within the project. While previous studies have been dedicated to the comparison [1][2] and optimisation [3] of guidance laws, this paper is entirely focused on the design of robust control compensators.

In fact, significant room for improvement can be achieved at this level since D&L control compensation is conventionally over-simplified or even non-existent, which is only practical if the target body is well-known or if guidance

algorithms do not rely on its natural dynamics. The application of robust control techniques is nowadays a well-established industrial practice for spacecraft attitude control design (e.g. [4][5]), but not so much for orbital control. This paper aims therefore to address the latter point. This approach is further motivated by, and based on, the recently-developed structured  $\mathcal{H}_\infty$  framework [6][7], which is particularly suitable for industry-oriented applications.

The paper is organised as follows: Sec. II introduces the Phobos benchmark under consideration, Sec. III describes the development of models that capture the D&L dynamics and uncertainties, Sec. IV is then dedicated to the synthesis of structured robust control compensators and Sec. V to their analytical and Monte-Carlo robustness assessment.

## II. PHOBOS MISSION BENCHMARK

Landing on Phobos is particularly challenging because of its reduced mass (8 orders of magnitude smaller than Mars) and proximity to the red planet (mean orbital altitude about 6000 km), which causes the planet's sphere of influence to end just 3.5 km above Phobos' surface. Hence, there is no possibility for Keplerian orbits around Phobos and the third-body perturbation of Mars cannot be neglected. Furthermore, due to the irregular shape and mass distribution of Phobos, the gravity of the moon cannot be accurately accounted for by a spherical field, thus it has to be described using a gravity harmonics (GH) model. In this case, using spherical coordinates  $(r, \theta, \phi)$  for distance to barycentre, co-latitude and longitude, as well as  $R$  for a reference radius and  $\mu_g$  for the gravitational constant, the gravity potential is given by [8]:

$$U_g(r, \theta, \phi) = \frac{\mu_g}{R} \sum_{n=0}^{\bar{n}} \left(\frac{R}{r}\right)^{n+1} \sum_{m=0}^n C_n^m(\phi) P_n^m(\cos \theta) \quad (1)$$

where  $P_n^m(x)$  are the associated Legendre polynomials and:

$$C_n^m(\phi) = C_{n,m} \cos m\phi + S_{n,m} \sin m\phi \quad (2)$$

is the expansion of the GH coefficients  $C_{n,m}$  and  $S_{n,m}$ . For Phobos,  $\bar{n} = 4$  (i.e., 28 coefficients) is assumed to suffice. However, 19 of these coefficients are highly inaccurately known. In fact, each of them is affected by a Gaussian dispersion with standard deviation equal to its mean value.

Given the small eccentricity of Phobos' orbit around Mars (approximately 0.015), the nonlinear dynamics of a spacecraft in the vicinity of the Mars-Phobos system is typically described as a circular restricted three-body problem. In this case, its motion can be written in a body-centred body-fixed (BCBF) frame with origin at the moon's barycentre as [1]:

$$\begin{bmatrix} \dot{\mathbf{r}}(t) \\ \dot{\mathbf{v}}(t) \\ \dot{\nu}(t) \end{bmatrix} = \mathbf{f}(\mathbf{r}(t), \mathbf{v}(t), \nu(t)) + \begin{bmatrix} 0_{3 \times 3} \\ I_{3 \times 3} \\ 0_{1 \times 3} \end{bmatrix} \mathbf{a}(t) \quad (3)$$

\*This work is funded by the UK Space Agency through a 2016 NSTP-2 Space Technology Fast Track grant entitled "Robust and Nonlinear Guidance and Control for Landing on Small Bodies". Mr. Simplicio is also the recipient of a Doctoral Training Partnership award by the UK EPSRC.

<sup>1</sup>Technology for Aerospace Control (TASC) Group, University of Bristol, Queen's Building, University Walk, Bristol BS8 1TR, UK, pedro.simplicio/andres.marcos@bristol.ac.uk

<sup>2</sup>Airbus Defence and Space, Gunnels Wood Road, Stevenage SG1 2AS, UK, eric.joffre@airbus.com

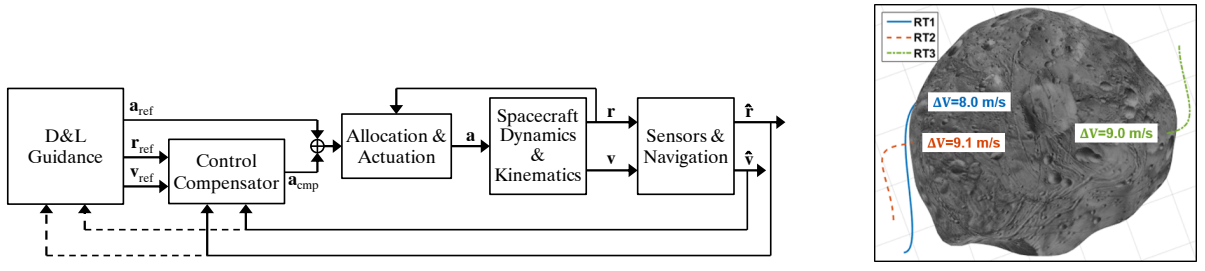


Fig. 1. Reference GNC architecture (left) and D&L trajectories (right) with corresponding value of  $\Delta V$

where the state vector  $[\mathbf{r}(t) \ \mathbf{v}(t) \ \nu(t)]^T$  gathers the position and velocity of the spacecraft with respect to Phobos, as well as the true anomaly of the latter around Mars, and the control vector  $\mathbf{a}(t)$  represents any propulsive acceleration generated by the spacecraft in the BCBF frame. It shall be noted that the vector field  $\mathbf{f}(\mathbf{r}(t), \mathbf{v}(t), \nu(t))$  can become extremely complex since it has to account for: [i] the three gravity forces as per Eq. (1) of Mars on Phobos, of Mars on the spacecraft and of Phobos on the spacecraft, [ii] non-inertial effects due to the rotation of the BCBF frame and [iii] propagation of the true anomaly of Phobos for the computation of its position.

In this benchmark, the behaviour of the spacecraft is simulated using the block diagram in Fig. 1, where the "spacecraft dynamics & kinematics" (SDK) model describes the relative motion of Eq. (3). For "D&L guidance" logics, two paradigms can be defined: [i] open-loop, employed when a reference trajectory  $\{\mathbf{r}_{\text{ref}}(t), \mathbf{v}_{\text{ref}}(t)\}$  and thruster profile  $\mathbf{a}_{\text{ref}}(t)$  are generated before and remain unchanged during the descent, or [ii] closed-loop, which refers to the case when the thruster profile is computed in real-time to correct the trajectory based on onboard measurements (as shown in Fig. 1 by the dashed lines).

Regardless of the type of guidance that precedes it, the architecture may be augmented with a "control compensator", which introduces an additional acceleration vector command  $\mathbf{a}_{\text{cmp}}(t)$  to further alleviate trajectory errors. As anticipated in Sec. I, the design of such a control compensator is the main focus of this paper. For synthesis and analysis purposes, three reference trajectories (RTs) [1] have been designed. These trajectories are also provided in Fig. 1, together with their nominal propellant requirements in terms of  $\Delta V$ .

### III. SPACE D&L SUBSYSTEM MODELLING

This section introduces the D&L subsystem models developed for control design. It covers the spacecraft dynamics in the vicinity of Mars-Phobos system (Sec. III-A), the inclusion of gravitational uncertainties via linear fractional transformations (LFTs) (Sec. III-B) and the definition of actuator/navigation models (Sec. III-C).

#### A. Orbital perturbation theory

For control design purposes, it is convenient to have a linear representation of Eq. (3), which is achieved via linearised orbital perturbation theory [9]. According to this theory, state and control variables can be defined at different operating points along a given trajectory as the sum of a reference (desired) value and small perturbations (deviations). The dynamics of these perturbations is then approximated

by the 1<sup>st</sup> order terms of the Taylor series expansion of  $\mathbf{f}(\mathbf{r}(t), \mathbf{v}(t), \nu(t))$  from Eq. (3) around the reference points:

$$\begin{bmatrix} \delta \dot{\mathbf{r}}(t) \\ \delta \dot{\mathbf{v}}(t) \\ \delta \dot{\nu}(t) \end{bmatrix} = \mathbf{J}_{\mathbf{f}}(t) \begin{bmatrix} \delta \mathbf{r}(t) \\ \delta \mathbf{v}(t) \\ \delta \nu(t) \end{bmatrix} + \begin{bmatrix} 0_{3 \times 3} \\ I_{3 \times 3} \\ 0_{1 \times 3} \end{bmatrix} \delta \mathbf{a}(t) \quad (4)$$

in which the Jacobian matrix given by:

$$\mathbf{J}_{\mathbf{f}}(t) = \begin{bmatrix} \frac{\partial \mathbf{f}}{\partial \mathbf{r}} & \frac{\partial \mathbf{f}}{\partial \mathbf{v}} & \frac{\partial \mathbf{f}}{\partial \nu} \end{bmatrix} \bigg|_{\substack{\mathbf{r} = \mathbf{r}_{\text{ref}}(t) \\ \mathbf{v} = \mathbf{v}_{\text{ref}}(t) \\ \nu = \nu_{\text{ref}}(t)}} \quad (5)$$

is computed via finite differences due to the complexity of  $\mathbf{f}(\mathbf{r}(t), \mathbf{v}(t), \nu(t))$ . Performing this linearisation at different instants of time  $t_i$ ,  $i = \{1, \dots, N\}$  along a reference trajectory allows to generate a set of linear time-invariant (LTI) SDK models  $G_{\text{SDK}}^i(s)$ :

$$\begin{bmatrix} \dot{\mathbf{x}}_{\text{SDK}}(s) \\ \delta \mathbf{r}(s) \\ \delta \mathbf{v}(s) \end{bmatrix} = \begin{bmatrix} \mathbf{J}_{\mathbf{f}}^i & \begin{bmatrix} 0_{3 \times 3} \\ I_{3 \times 3} \\ 0_{1 \times 3} \end{bmatrix} \\ I_{6 \times 6} & 0_{6 \times 1} \end{bmatrix} \begin{bmatrix} \mathbf{x}_{\text{SDK}}(s) \\ \delta \mathbf{a}(s) \end{bmatrix} \quad (6)$$

where  $\mathbf{J}_{\mathbf{f}}^i = \mathbf{J}_{\mathbf{f}}(t_i)$  is a constant matrix given by Eq. (5) and  $\mathbf{x}_{\text{SDK}}(s)$  is the internal state vector.

#### B. Inclusion of gravitational uncertainties

As introduced in Sec. II, 19 GH coefficients are highly inaccurately known, which means that the computation of  $\mathbf{J}_{\mathbf{f}}^i$  in Eq. (5) is subject to a high level of uncertainty. To capture the effect of this uncertainty, a mathematical representation known as linear fractional transformation (LFT) [10] is employed. Using this approach, it is common to isolate what is known as an LTI system  $M(s)$  and gather all the "trouble-making" (uncertain, time-varying or nonlinear) components into an operator  $\Delta_{\mathbf{x}} = \text{diag}(\delta_{x_1}, \delta_{x_2}, \dots, \delta_{x_n})$ , bounded as  $\|\Delta_{\mathbf{x}}\|_{\infty} \leq 1$ . LFTs are particularly attractive because typical algebraic operations preserve the LFT structure.

To build representative  $G_{\text{SDK}}^i(s)$  LFT models, the following procedure (to be repeated for every  $t_i$ ) has been adopted:

- 1) To minimise the size of the resulting LFT, only the GH coefficients with higher impact on  $\mathbf{J}_{\mathbf{f}}^i$  are selected and denoted  $\rho_{\text{GH}}$ . For this choice, two criteria are applied: impact of each coefficient on the nonlinear simulation of Eq. (3) and relative weight of each coefficient on dedicated interpolations (refer to next step).
- 2) An appropriate number of dispersed samples is then generated and the Jacobian matrix in Eq. (5) is evaluated for each sample. Here, two cases are considered:

$2\sigma$  and  $3\sigma$  dispersions, capturing respectively 95.5% and 99.7% of uncertainty. For each case, a matrix with polynomial dependence on the uncertain parameters  $J_f^i(\rho_{GH})$  is then interpolated, which is accomplished using the orthogonal least-squares approximation routine of ONERA's APRICOT library [11].

- 3) The LTI system of Eq. (6) with  $J_f^i(\rho_{GH})$  is finally converted into an LFT also via the APRICOT library, which adjusts the necessary repetitions of each coefficient in  $\rho_{GH}$  to meet a pre-specified approximation error. It is therefore reasonable that its size changes with the level of conservativeness and also along the trajectory. This behaviour is depicted in Fig. 2.

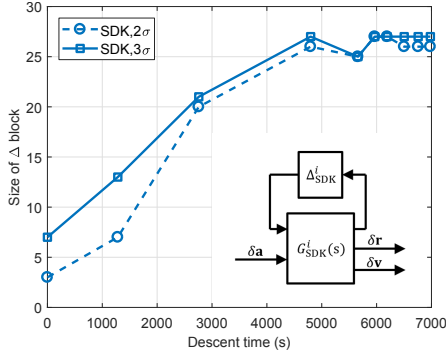


Fig. 2. SDK LFT and size of  $\Delta_{\text{SDK}, 2\sigma}^i(s)$  and  $\Delta_{\text{SDK}, 3\sigma}^i(s)$  along RT1

### C. Actuator and navigation models

The "allocation & actuation" block in Fig. 1 is responsible for the introduction of thruster realisation errors. These errors are time and trajectory dependent, but they are assumed to be bounded. Therefore, this effect can be naturally captured using a simple LFT model  $G_A(s)$  and uncertainty block  $\Delta_A(s) = \text{diag}(\delta_{ax}, \delta_{ay}, \delta_{az}, I_{3 \times 3} \delta_{aod})$ . Here,  $\delta_{ax}, \delta_{ay}, \delta_{az}$  are uncertainties affecting the three axes and  $\delta_{aod}$  represents off-diagonal effects. Note that the relative ranges of  $\Delta_A(s)$  have been established from Monte-Carlo simulations and normalised to  $[-1, 1]$  with  $M(s)$  absorbing the scaling factor. Since ranges are relative,  $G_A(s)$  is applicable to both full  $\mathbf{a}_{\text{cmd}}(t)$  and perturbed  $\delta \mathbf{a}_{\text{cmd}}(t)$  commands.

The "sensors & navigation" algorithms introduce two different effects: a quantisation and a noise error. The former effect is due to the fact that position and velocity estimates,  $\hat{\mathbf{r}}(t)$  and  $\hat{\mathbf{v}}(t)$ , are updated every 60 s, which is sufficient given the slow dynamics of the spacecraft, but injects a non-smooth signal. To attenuate it, estimates are filtered by a first-order low-pass filter  $G_{\text{LPF}}(s)$  with 0.05 Hz bandwidth. The noise error is accounted for by colouring white noise signals  $\mathbf{n}_r(t)$  and  $\mathbf{n}_v(t)$  through first-order transfer functions  $G_{\text{rNAV}}(s)$  and  $G_{\text{vNAV}}(s)$  such that the frequency content produced by the nonlinear "sensors & navigation" is recovered. These filters are equally applicable to full and perturbed estimates since  $\mathbf{r}_{\text{ref}}(t)$  and  $\mathbf{v}_{\text{ref}}(t)$  are known without error.

## IV. STRUCTURED ROBUST CONTROL SYNTHESIS

This section is dedicated to the synthesis of robust control compensators using structured  $\mathcal{H}_\infty$  optimisation, starting with a brief overview of this paradigm in Sec. IV-A. Its application to the D&L problem is illustrated in Sec. IV-B and nominal results are shown in Sec. IV-C.

### A. The structured $\mathcal{H}_\infty$ framework

The structured  $\mathcal{H}_\infty$  paradigm has been first proposed as an alternative to tackle the main practical limitation of standard  $\mathcal{H}_\infty$  optimisation, namely its inability to constrain controller size or structure by design. This algorithm is part of the *hinfstruct* and *systune* routines of MATLAB [6] and is nowadays able to seamlessly account for parametric plant uncertainties [7]. As the name indicates, the control problem remains the same - an  $\mathcal{H}_\infty$ -norm minimisation of the LFT:

$$\|\mathcal{F}_u\{M(s), \Delta(s)\}\|_\infty < 1 \quad (7)$$

but, thanks to a rearranged formulation, it enables the combined handling of multiple requirements, as well as design plants. The latter feature is particularly valuable for the D&L problem since it allows to synthesise controllers that are valid not only for one, but for a set of points in Space.

Naturally, these advantages come at the expense of a challenging (non-smooth) mathematical problem. To solve it, structured  $\mathcal{H}_\infty$  employs local optimisation methods, hence the initialisation of the algorithm may become of critical relevance, which was not the case with standard  $\mathcal{H}_\infty$ . Nonetheless, its ability to specify controller structure and hence take advantage of industry-legacy knowledge makes structured  $\mathcal{H}_\infty$  a very successful approach and applications to Space [12][13] and Aeronautics [14] have already flown.

### B. Application of structured $\mathcal{H}_\infty$ to D&L compensation

As introduced in Sec. II, the objective of the control compensator is to provide an additional acceleration command  $\mathbf{a}_{\text{cmp}}(t)$  to compensate for deviations with respect to a RT. The structure chosen for this compensator is shown in Fig. 3.

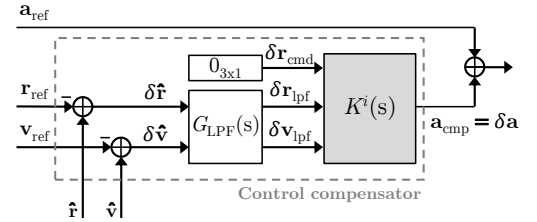


Fig. 3. Control compensator architecture

At the core of the compensator, there is an LTI controller  $K^i(s)$  that must be designed to track commanded deviations  $\delta \mathbf{r}_{\text{cmd}}(t)$  using position and velocity deviation measurements  $\delta \hat{\mathbf{r}}(t)$  and  $\delta \hat{\mathbf{v}}(t)$  with respect to a given RT, filtered by  $G_{\text{LPF}}(s)$  (Sec. III-C). An additional command  $\delta \mathbf{v}_{\text{cmd}}(t)$  could have been included, but it was found to be redundant and hence not considered. With such a structure, the controller can be designed based on the orbital perturbation model (Sec. III-A) by realising that the acceleration command is actually a perturbation, i.e.,  $\mathbf{a}_{\text{cmp}}(t) = \delta \mathbf{a}(t)$ . The closed-loop interconnection is depicted in Fig. 4 (left), which includes the actuator/navigation blocks of Sec. III-C and the SDK LFT of Sec. III-B. Here, the superscript  $i = \{1, \dots, 10\}$  specifies different points along the RT and  $*$  represents  $2\sigma$  or  $3\sigma$ , depending on the LFT conservativeness.

Generically speaking, a different LTI controller  $K^i(s)$  can be synthesised for each design point  $i$  but, with the capabilities of *hinfstruct* (Sec. IV-A), a single multi-plant controller  $K(s)$  can be synthesised so as to fulfil control

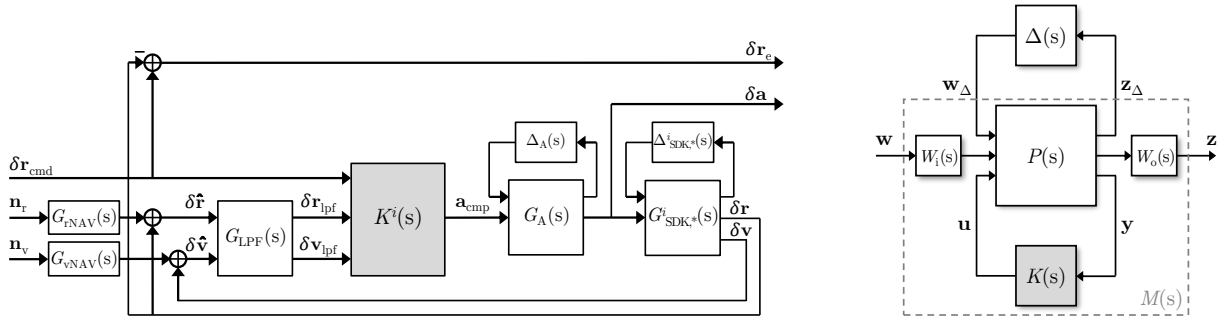


Fig. 4. Closed-loop model (left) and generalised interconnection (right) for control synthesis

requirements at all the design points  $i = \{1, \dots, 10\}$ . Requirements are posed by rearranging the problem as in Fig. 4 (right) and defined through frequency-dependent weights  $W_i(s)$  and  $W_o(s)$ . For this problem, weights were chosen the same for all the design points. Weight  $W_i(s)$  is employed for a differential scaling within the signal  $\mathbf{w}(s) = [\delta \mathbf{r}_{\text{cmd}}(s); \mathbf{n}_r(s); \mathbf{n}_v(s)]$ . For this specific case, with main focus on the effect of GH uncertainties, no noise has been considered, thus  $W_i(s) = \text{diag}(I_{3 \times 3}, 0_{3 \times 3}, 0_{3 \times 3})$ . The weight  $W_o(s)$ , applied to signal  $\mathbf{z}(s) = [\delta \mathbf{r}_e(s); \delta \mathbf{a}(s)]$ , is partitioned as  $W_o(s) = \text{diag}(W_S(s), W_A(s))$ , where  $W_S(s)$  and  $W_A(s)$  impose tracking and actuation requirements.

More specifically, as a consequence of Eq. (7), the response of  $\delta \mathbf{r}_e(s)$  shall be bounded by  $W_S^{-1}(s)$ , hence this inverse shall have [i] small low-frequency gain ( $10^{-3}$ ) for little static error, [ii] reasonable high-frequency gain (2) for good stability margins and [iii] roll-over frequency ( $10^{-2}$  rad/s) appropriate for the problem. Similarly,  $\delta \mathbf{a}(s)$  is bounded by  $W_A^{-1}(s)$  and the inverse shall have [i] reasonable low-frequency gain ( $5.5 \times 10^{-4}$ ) establishing maximum control effort, [ii] small high-frequency gain ( $10^{-9}$ ) for little reactivity to noisy signals, [iii] roll-off frequency ( $10^{-3}$  rad/s) able to accommodate the tracking bandwidth.

Following the multi-plant approach, plants at different design points are aggregated in a block-diagonal structure and the *hinfstruct* routine is called to find a single stabilising controller. As mentioned in Sec. IV-A, this routine is nowadays able to account for parametric uncertainties  $\Delta^i(s)$  in the optimisation problem. In the same section, it is anticipated that the initialisation and choice of tuneable parameters may be critical for the success of the optimisation. Here, a third-order controller was chosen with the off-diagonal terms of its state-space matrices fixed to zero and with reasonable initial guesses for the remaining terms. As a consequence, the highly-coupled D&L dynamics will be tackled by a diagonal (but robust) controller with 24 tuneable parameters.

Following this strategy, four controllers have been designed:  $K_0$  (not accounting for any uncertainties),  $K_A$  (accounting for  $\Delta_A$  only),  $K_{A,2\sigma}$  (accounting for  $\Delta_A$  and  $\Delta_{\text{SDK},2\sigma}^i$ ) and  $K_{A,3\sigma}$  (accounting for  $\Delta_A$  and  $\Delta_{\text{SDK},3\sigma}^i$ ).

### C. Nominal results

Before proceeding to an in-depth robustness analysis, the nominal behaviour of the designed controllers is analysed. All of them perform very similarly under nominal conditions, thus only results concerning  $K_{A,2\sigma}$  are shown in this section. Fig. 5 shows the singular values of  $\delta \mathbf{r}_e(s)$  and  $\delta \mathbf{a}(s)$  channels

against the corresponding  $\mathcal{H}_\infty$  constraints  $W_S^{-1}(s)$  (top) and  $W_A^{-1}(s)$  (bottom) along RT1 (in different colours).

From here, it is clear that, in nominal conditions, design requirements are met for all the points throughout RT1, although margins with respect to  $W_S^{-1}(s)$  and  $W_A^{-1}(s)$  become more challenging closer to touchdown. A distinction is also made between diagonal and off-diagonal terms (continuous and dashed lines), which shall be as separate as possible to minimise cross-coupled interactions.

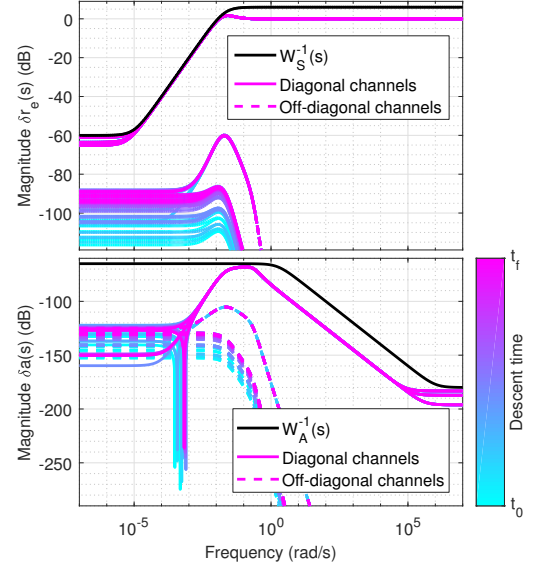


Fig. 5. Multi-channel singular values along RT1 and  $t_i \in [t_0, t_f]$  against  $W_S^{-1}(s)$  (top) and  $W_A^{-1}(s)$  (bottom) using controller  $K_{A,2\sigma}$

In addition, to demonstrate the effect of control compensation, a nonlinear simulation of RT1 is depicted in Fig. 6, showing trajectory and arrows with magnitude and direction of acceleration reference  $\mathbf{a}_{\text{ref}}(t)$ , compensation  $\mathbf{a}_{\text{cmp}}(t)$ , and total signal (i.e.,  $\mathbf{a}_{\text{ref}}(t) + \mathbf{a}_{\text{cmp}}(t)$ ). The compensator command is clearly visible, with smaller magnitude than the reference vector, but enough to correct it and track the desired trajectory.

### V. ROBUSTNESS ANALYSIS AGAINST UNCERTAINTIES

In this section, the impact of gravitational uncertainties when using different compensators is assessed. This assessment is carried out both analytically via the structured singular value  $\mu$  (introduced in Sec. V-A and applied in Sec. V-B) and through Monte-Carlo (MC) simulation (Sec. V-C).



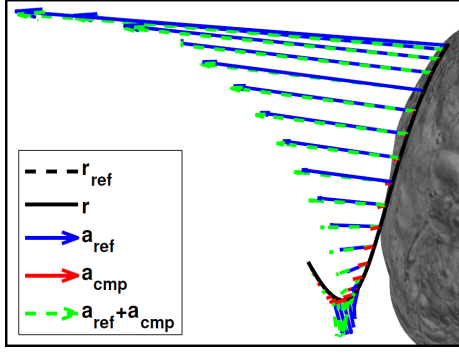


Fig. 6. Nonlinear simulation of RT1 using controller  $K_{A,2\sigma}$

#### A. The $\mu$ analysis framework

The fundamental approach for analytical system robustness assessment is based on the structured singular value  $\mu$  [10]. Without uncertainties, nominal performance (NP) is assessed by verifying if Eq. (7) holds for  $\Delta = 0$ . Under the presence of the uncertainties bounded as  $\|\Delta\|_\infty \leq 1$ , robust performance (RP) is assessed through:

$$\mu(M) = \frac{1}{\min_{\Delta_p} \{\bar{\sigma}(\Delta_p) : \det(I - M\Delta_p) = 0\}} \quad (8)$$

where  $\Delta_p$  corresponds to the block  $\Delta$  augmented with a fictitious uncertainty that closes the input/output channels of  $M(s)$  and  $\bar{\sigma}(\Delta_p)$  represents its maximum singular values. Smaller values of  $\mu(M)$  indicate better RP properties and all the requirements are fulfilled if and only if  $\mu(M) < 1$ . Moreover, the norm of the smallest set of uncertainties that maximises  $\mu(M)$  is given by  $\|\mu(M)\|_\infty^{-1}$ . The computation of Eq. (8) is NP-hard, hence its estimation relies on lower and upper bounds. Robust stability (RS) can also be verified via  $\mu$  analysis but, since RS is not of concern for any of the controllers, it is not addressed here.

#### B. Application of $\mu$ analysis to D&L compensation

An overview of all the information provided by  $\mu$  analysis is illustrated in Fig. 7 (shown in the next page for clarity) for point  $i = 8$ , which corresponds to a descent time around 6500 s. On the top plots, curves related to the NP and RP tests are depicted (there are actually two lines for RP representing lower and upper bounds of  $\mu$ ). On the bottom, the sensitivity of RP results against each element of  $\Delta$  (directly computed with  $\mu$  algorithms) is also plotted. A higher sensitivity indicates that the corresponding uncertainty has a stronger impact on the solution found with  $\mu$ .

The left-most column shows the closed-loop analysis with  $K_A$  against the effect of  $\Delta_A$ . Since NP and RP curves lie below 1, the corresponding conditions are met in this case, which is natural as the uncertainties considered for design and analysis are the same. NP is more demanding at low and very high-frequency, which could be anticipated from the proximity of the closed-loop responses in Fig. 5 with the  $W_S^{-1}(s)$  and  $W_A^{-1}(s)$  curves. Performance degradation caused by the presence of uncertainties is then translated by RP indicators larger than NP.

The central plots of Fig. 7 show the same analysis with  $K_A$ , but now against the combined effect of actuator and GH uncertainties,  $[\Delta_A; \Delta_{SDK,3\sigma}^8]$ . As expected, considering

a wider range of uncertainties leads to the same NP, but degraded RP, now approaching unity. Also, the elements of  $\Delta_{SDK,3\sigma}^8$  are now included in the sensitivities plot. In fact, the impact of these elements becomes comparable to that of  $\Delta_A$ , precisely at low-frequency where RP is worse.

The right column then shows the results against the same set of uncertainties  $[\Delta_A; \Delta_{SDK,3\sigma}^8]$ , but now replacing the controller with  $K_{A,3\sigma}$ . This leads to NP and RP conditions being met by a change of closed-loop behaviour at low-frequency. However, sensitivity frequency responses remain roughly the same, which indicates that this type of insight is not intrinsically dependent on the controller being analysed.

#### C. Monte-Carlo verification

The robustness of the four controllers designed in Sec. IV-B is now verified via nonlinear MC simulation by comparing results of the same 2000 samples of the 19 GH coefficients in Eq. (2) (randomly sampled with Gaussian distributions). In addition, verification is complemented with worst-cases (WCs) that correspond to the combination of uncertainties associated with RP peaks (analytically identified via  $\mu$  analysis, at every design point). Since not all of the GH coefficients are captured by the LFTs, every combination is tested with the remaining coefficients set to their nominal,  $+3\sigma$  and  $-3\sigma$  values. Hence, these WCs are expected to have a very low probability of occurrence, but to be more challenging than the remaining MC runs.

The outcome of this campaign is illustrated in Fig. 8 for RT1 and  $K_{A,2\sigma}$ , highlighting distance and speed errors with respect to the RT, magnitude of the acceleration compensation command and total  $\Delta V$  (i.e., reference plus compensation). The average and standard deviation of the maximum values of these indicators using the different controllers are then listed in Table I. For clarity, failure cases (i.e., spacecraft crashing on or diverging from Phobos) are not shown in the plots, but are accounted for in the table.

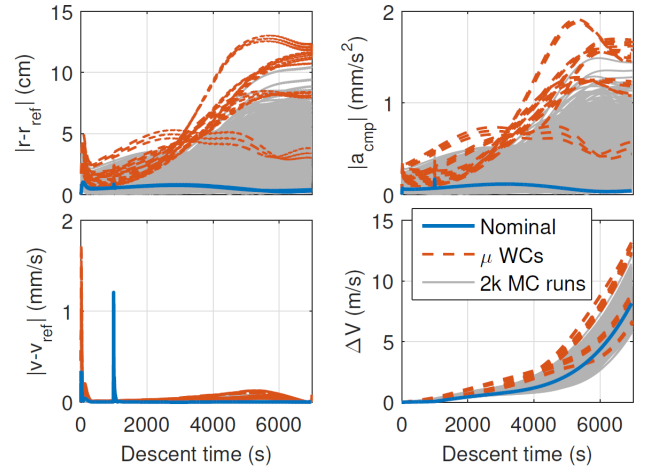


Fig. 8. Nonlinear simulation of 2000 Monte-Carlo runs and worst cases from  $\mu$  analysis of RT1 using  $K_{A,2\sigma}$

As expected, the non-robust controller  $K_0$  is not suitable for this scenario since it yielded MC and WC failure ratios of 44.15 and 33.33%. The three robust controllers then showed satisfactory and equivalent distribution indicators, but distinct failure ratios. With  $K_A$ , no failures were obtained from the MC simulations, but 12.5% of the  $\mu$  WCs resulted in failure.

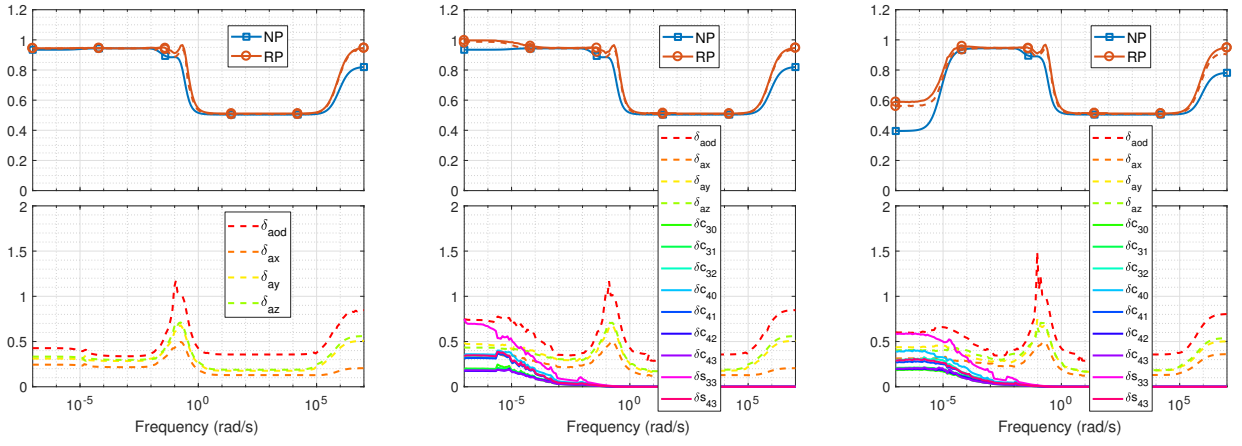


Fig. 7.  $\mu$  bounds (top) and sensitivities (bottom) at  $i=8$  using  $K_A$  w/  $\Delta_A$  (left),  $K_A$  w/  $[\Delta_A; \Delta_{\text{SDK},3\sigma}^8]$  (centre) and  $K_{A,3\sigma}$  w/  $[\Delta_A; \Delta_{\text{SDK},3\sigma}^8]$  (right)

TABLE I

ROBUSTNESS INDICATORS FOR RT1 USING DIFFERENT CONTROLLERS

	$K_0$		$K_A$		$K_{A,2\sigma}$		$K_{A,3\sigma}$	
Max. MC values	Avg.	Std.	Avg.	Std.	Avg.	Std.	Avg.	Std.
$ \mathbf{r} - \mathbf{r}_{\text{ref}} $ (m)	0.503	0.259	0.029	0.013	0.030	0.014	0.038	0.020
$ \mathbf{v} - \mathbf{v}_{\text{ref}} $ (mm/s)	1.234	0.130	1.206	0.008	1.208	0.007	1.212	0.013
$ \mathbf{a}_{\text{cmp}} $ (mm/s <sup>2</sup> )	0.411	0.207	0.431	0.208	0.430	0.208	0.429	0.206
$\Delta V$ (m/s)	8.793	0.630	8.326	0.966	8.326	0.965	8.329	0.955
MC failures (%)	44.15		0.00		0.00		0.10	
WC failures (%)	33.33		12.50		0.00		16.67	

The situation was improved with  $K_{A,2\sigma}$ , where there was no MC or WC failure. Finally, results using  $K_{A,3\sigma}$  became inferior, with failure ratios of 0.1 and 16.37%. Although this last result may seem counter-intuitive, it is actually a fairly common pitfall of robust control algorithms, in which performance becomes restricted in case of an over-conservative uncertainty specification during the design phase.

With this in mind,  $K_{A,2\sigma}$  is selected as the most suitable compensator. In order to assess its applicability to trajectories other than the one it has been designed for, the same MC campaigns are executed for RT2 and RT3 (recall Fig. 1) and the corresponding indicators are gathered in Table II. Since no detailed  $\mu$  analysis was performed along RT2 or RT3, the consideration of WCs is not pursued here.

TABLE II

ROBUSTNESS INDICATORS FOR DIFFERENT TRAJECTORIES USING  $K_{A,2\sigma}$

	RT1		RT2		RT3	
Max. MC values	Avg.	Std.	Avg.	Std.	Avg.	Std.
$ \mathbf{r} - \mathbf{r}_{\text{ref}} $ (m)	0.030	0.014	0.026	0.010	0.026	0.011
$ \mathbf{v} - \mathbf{v}_{\text{ref}} $ (mm/s)	1.208	0.007	0.694	0.253	0.661	0.325
$ \mathbf{a}_{\text{cmp}} $ (mm/s <sup>2</sup> )	0.430	0.208	0.332	0.160	0.326	0.164
$\Delta V$ (m/s)	8.326	0.965	8.714	0.831	7.989	0.830
MC failures (%)	0.00		0.00		0.00	

The results of Table II show that the D&L runs along RT2 and RT3 have been executed with similar performance to RT1 and also without any failure. This conclusion shows that accounting for the uncertainties encountered along RT1 alone turned out to be enough for the design of a compensator that is equally able to cope with other trajectories.

## VI. CONCLUSIONS

This paper illustrated how LFT modelling and structured  $\mathcal{H}_\infty$  synthesis can be effectively adopted to design simple yet robust control compensators for Space D&L. This in turn

paves the way for more efficient guidance strategies and more reliable planetary landers. While doing so, emphasis was placed on the main strengths of the structured  $\mathcal{H}_\infty$  method, namely its ability to handle multiple plants, as well as on its challenges, mostly related to its potential sensitivity to initial conditions. Finally, it was shown how  $\mu$  analysis can be directly employed to support the design process and also as a complement to more conventional Monte-Carlo verification.

## REFERENCES

- [1] E. Joffre, M. Zamaro, N. Silva, A. Marcos, P. Simplicio, and B. Richardson, "Landing on Small Bodies Trajectory Design, Robust Nonlinear Guidance and Control," in *The 27th AAS/AIAA Spaceflight Mechanics Meeting*, San Antonio, TX, Feb 5–9 2017.
- [2] P. Simplicio, A. Marcos, E. Joffre, M. Zamaro, and N. Silva, "Parameterised Laws for Robust Guidance and Control of Planetary Landers," in *The 4th EuroGNC Conference*, Warsaw, Poland, Apr 25–27 2017.
- [3] —, "A Systematic Performance-oriented Tuning for Space Exploration Descent & Landing Guidance," in *The 7th European Conference for Aeronautics and Space Sciences*, Milan, Italy, Jul 3–6 2017.
- [4] C. Charbonnel, " $\mathcal{H}_\infty$  Controller Design and  $\mu$ -Analysis: Powerful Tools for Flexible Satellite Attitude Control," in *The 2010 AIAA Guidance, Navigation, and Control Conference*, Toronto, Canada, Aug 2–5 2010.
- [5] M. Watt, M. Yu, A. Falcoz, P. Singh, and C. Warren, "BIOMASS Normal Mode AOCS: Classical versus Robust Design," in *The 8th International ESA Conference on Guidance, Navigation and Control Systems*, Karlovy Vary, Czech Republic, Jun 5–10 2011.
- [6] P. Gahinet and P. Apkarian, "Structured  $\mathcal{H}_\infty$  Synthesis in MATLAB," in *The 18th IFAC World Congress*, Milan, Italy, Aug 28–Sep 2 2011.
- [7] P. Apkarian, M. Dao, and D. Noll, "Parametric robust structured control design," *Transactions on Automatic Control*, vol. 60, no. 7, pp. 1857–1869, 2015.
- [8] M. Zamaro and J. Biggs, "Natural motion around the Martian moon Phobos: the dynamical substitutes of the Libration Point Orbits in an elliptic three-body problem with gravity harmonics," *Celestial Mechanics and Dynamical Astronomy*, vol. 122, pp. 263–302, 2015.
- [9] R. Battin, *An Introduction to the Mathematics and Methods of Astrodynamics*, 1st ed. AIAA Education Series, 1987.
- [10] K. Zhou, J. Doyle, and K. Glover, *Robust and Optimal Control*, 1st ed. Prentice-Hall, 1995.
- [11] C. Roos, G. Hardier, and J.-M. Biannic, "Polynomial and rational approximation with the APRICOT Library of the SMAC toolbox," in *The 2014 IEEE Conference on Control Applications*, Antibes, France, Oct 8–10 2014.
- [12] A. Falcoz, C. Pittet, S. Bennani, A. Guignard, C. Bayart, and B. Frapard, "Systematic design methods of robust and structured controllers for satellites," *Space Journal*, vol. 7, no. 3, pp. 319–334, 2015.
- [13] C. Pittet and P. Prieur, "Structured accelero-stellar estimator for MICROSCOPE drag-free mission," in *The 3rd EuroGNC Conference*, Toulouse, France, Apr 13–15 2015.
- [14] A. Marcos and M. Sato, "Flight Testing of a Structured  $\mathcal{H}_\infty$  Controller: a EU-Japan Collaborative Experience," in *The 1st IEEE Conference on Control Technology and Applications*, Kohala Coast, HI, Aug 27–30 2017.